

Chapter 1

Optical wireless broadcast system design

1.1 SVD-VLC System Design

1.1.1 Singular Value Decomposition - Native System

The SVD technique applies coordinate system transformations on correlated channels and generates simultaneous independent links and maximizes the capacity of the MIMO channel when the CSI is known at the transmitter and the receiver. The channel matrix \mathbf{H} can be decomposed into rotation and scaling matrices using SVD as

$$\mathbf{H} = \mathbf{U}\mathbf{\Lambda}\mathbf{V}^* \quad (1.1)$$

\mathbf{U} and \mathbf{V} are unitary rotation matrices while $\mathbf{\Lambda}$ is a diagonal scaling matrix. Matrices \mathbf{H} and $\mathbf{\Lambda}$ have the same rank $\Gamma \leq \min(N_{tx}, N_{px})$. The diagonal elements of $\mathbf{\Lambda}$ ($\lambda_1 \dots \lambda_k \dots \lambda_\Gamma$) are the singular values of matrix \mathbf{H} and the squared singular values are the eigenvalues of $\mathbf{H}\mathbf{H}^*$. Now let us define new variables in rotated coordinate systems as

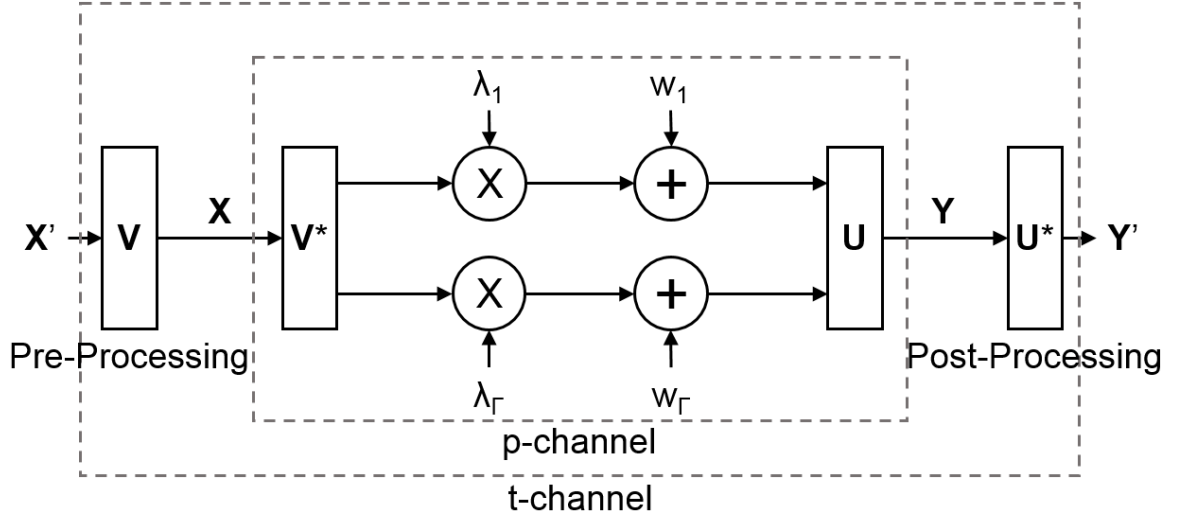


Figure 1.1: Native SVD System Block Diagram¹

$$\mathbf{X}' := \mathbf{V}^* \mathbf{X} \quad (1.2)$$

$$\mathbf{Y}' := \mathbf{U}^* \mathbf{Y} \quad (1.3)$$

$$\mathbf{W}' := \mathbf{U}^* \mathbf{W} \quad (1.4)$$

Inserting the above definitions in MIMO channel model and then pre-multiplying both sides by \mathbf{U}^* transforms the MIMO channel model as

$$\mathbf{Y}' = \mathbf{\Lambda} \mathbf{X}' + \mathbf{W}' \quad (1.5)$$

Figure 1.1 illustrates the transformed MIMO channel. \mathbf{X}' are the inputs for the data streams in the coordinate system defined by columns of \mathbf{V} and \mathbf{Y}' are the outputs in the coordinate system defined by columns of \mathbf{U} . Since \mathbf{U} is a unitary matrix, elements of \mathbf{W}' will be IID and have the same variance (noise power) as \mathbf{W} (Tse and Viswanath, 2005). Since $\mathbf{\Lambda}$ is a diagonal matrix, extracting the simultaneous

¹Adapted from (Tse and Viswanath, 2005), pg 292-293

equations from Eq.1.5 gives Γ simultaneous independent link models described by

$$y'_k = \lambda_k x'_k + w'_k; 1 \leq k \leq \Gamma \quad (1.6)$$

In RF MIMO systems, the aggregate transmit power is the binding constraint. The waterfilling algorithm (Goldsmith and Varaiya, 1997) provides a solution for allocate powers to the independent streams in order to maximize the channel capacity. As a result of this optimization, links with SNR greater than a threshold, are allocated power budget corresponding to their SNRs, while those with SNR below the threshold do not transmit any information. Let $\mathbf{K}'_{\mathbf{k}}$ be these waterfilling power allocations. Then the upper bound on the capacity of the channel is given by

$$C_{SVD} < \sum_{k=1}^{\Gamma} \log_2 \left(1 + \frac{\lambda_k^2 K'_k}{\sigma_{MIMO}^2 B} \right) \quad (1.7)$$

1.1.2 Singular Value Decomposition - VLC System

In the above model, the information streams are defined over inputs x'_k . Note $\lambda_k = 0; k > \Gamma$ and thus no information can be transmitted over those links. At the transmitters, transformation \mathbf{V} multiplexes the streams over the physical channel. At the receiver, transformation \mathbf{U}^* demultiplexes the independent streams. These transformations are also called pre-processing and post-processing.

An SVD architecture with different power and offset allocation has been proposed for MIMO VLC communications in (Park et al., 2011). In this work, the aggregate sum of average radiated optical flux from multiple LEDs is constrained to be smaller than or equal to an upper bound in order to fulfill the eye safety requirements. Under this condition, it is still possible for the system to inadvertently violate the eye safety limit if the channel matrix is not full rank despite satisfying the stated constraints. Alternately, the system will under-utilize the capacity of the channel. Also, the illumi-

nation generated by that system changes with the channel matrix thus transitioning to a different illumination state every time the channel matrix is changed. Finally, the solution restricts itself to M-PAM and necessitates different optimization for different modulation schemes.

Native SVD does not impose any form of non-negativity or illumination constraint. The SVD-VLC architecture is derived from the native SVD architecture to optimally utilize the capacity of the channel while satisfying illumination constraints. For indoor VLC system to provide illumination and optical wireless access simultaneously, the channel constraints are given by

Non-Negativity Constraint

For indoor VLC system, information is carried over an intensity signal which cannot be negative. 1.8 implies that input symbols should be defined to generate positive values after preprocessing.

$$\mathbf{X} \geq \mathbf{0} \leftrightarrow \mathbf{V}\mathbf{X}' \geq \mathbf{0} \quad (1.8)$$

Illumination Constraint

In an indoor space, a user can specify a desired illumination state. This specifies the average radiant flux to be emitted by each luminaire. Eq.1.9 states that the average radiant flux transmitted by each luminaire must equal the desired illumination state. Let \mathbf{P} be the vector that defines the average output radiant flux from each transmitter. Then \mathbf{P}' gives this constraint on the transformed links. This implies that the average signal value in the transformed space must be equal to the corresponding element of \mathbf{P}' .

$$E[\mathbf{X}] = \mathbf{P} \leftrightarrow \mathbf{P}' = E[\mathbf{X}'] = \mathbf{V}^*\mathbf{P} \quad (1.9)$$

It is worth noting that \mathbf{X}' must satisfy the equation for all its elements irrespective of the channel gain of the corresponding transformed link. This implies that when the channel matrix \mathbf{H} or $\mathbf{\Lambda}$ is not full rank, the SVD-VLC architecture still expects the transformed links whose channel gain $\lambda_k = 0$ to maintain an average signal level as specified by this constraint. So even though these transformed links carry no information, it is vital to satisfy the average signal constraint to service illumination.

Input Signal Ranges

Eq.1.10 specifies the set of values that \mathbf{X}' can take at any given instant of time provided the other constraints are satisfied.

$$M[\mathbf{X}' \cdot \text{sgn}(\mathbf{P}')] \geq \mathbf{0} \quad (1.10)$$

The above constraint states that the modulated signal for each luminaire can span either the non-negative or the non-positive but not both ranges of the Real number line as dictated by the illumination constraint.

SVD-VLC Architecture

Figure 1.2 illustrates SVD-VLC system architecture. The 'I1-streams' are the $N_{tx} - \Gamma$ links that service only illumination. The 'I2-streams' are the Γ information + illumination bearing links. The I1 and I2 streams are preprocessed by \mathbf{V} to transform and multiplex them over the channel. This multiplexing generates and maintains the desired illumination state in the indoor space. At the imaging receiver, the TIAs for each pixel add i.i.d white gaussian noise to each link. Postprocessing by \mathbf{U}^* demultiplexes the parallel links and recovers the Γ I2 streams. The streams can be jointly decoded to optimally recover the transmitted data. Thus the SVD-VLC architecture services the illumination while achieving high data rates over the VLC

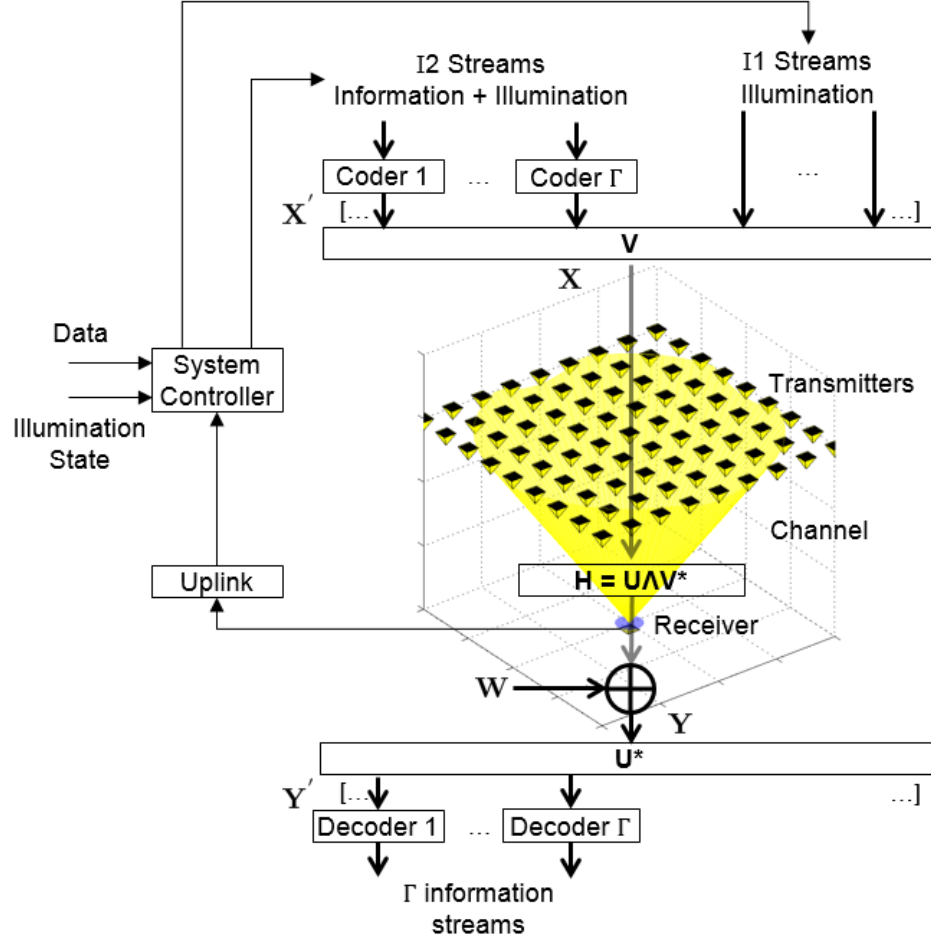


Figure 1.2: SVD-VLC System Block Diagram

channel.

The SVD architecture assumes that the CSI is known at the transmitter and the receiver. For my dissertation, I will investigate MIMO strategies when CSI is not known at transmitter. I also wish to analyze the capacity of the system when each luminaire has a maximum signal power constraint and peak amplitude constraints while maintaining illumination. The receiver can estimate the channel using pilot signals. I also propose the extend the SVD-VLC architecture to support mobile receivers and multiple users.

1.1.3 Analysis

The capacity of the MIMO channel with imaging receiver is analyzed and compared with an equivalent SISO channel. Table 1.1 outlines the system parameters used. For the MIMO channel, the luminaires are arranged in a grid at the a height of 3m in the room and at a pitch of D_{tx} . The luminaires are assumed to be point sources with enough output luminous flux to provide the desired illumination. The SPD of the emitted flux is approximated using sum of gaussians to that used in (Grubor et al., 2008). The receiver bandwidth is assumed to be 50 MHz (Zeng et al., 2008). For this analysis the receiver is always assumed located at the center of the length-width plane. The same sensor side length a_{rx} is maintaied for the SISO PD and the imaging receiver. The case where the aperture collection area of the imaging receiver is the same as the area of the SISO receiver is also considered.

Figure1-3 shows the theoretical capacity of the SISO and MIMO channels over

Table 1.1: VLC System Configuration Parameters

Parameter		Value	Units
Room Length	L_{rm}	4	m
Room Width	W_{rm}	4	m
Room Height	H_{rm}	4	m
Transmitter grid pitch ¹	D_{tx}	0.5	m
Total number of transmitters ¹	$N_{tx}^L \times N_{tx}^W$	9x9	-
Transmitter Lambertian Order	m	1	-
Optics Field of View	ψ_c^o	60	degrees
Optics focal length ¹	f	5	mm
Optics transmission ¹	Q	1	-
Concentrator refractive index ²	η	1.5	-
Ideal filter transmission	$T(\lambda)\forall\lambda$	1	-
Sensor Side length	a_{rx}	5	mm
Pixel side length ¹	α_{rx}	1	mm
Pixel pitch ¹	δ_{rx}	1	mm
Total number of pixels ¹	$N_{px}^L \times N_{px}^W$	5x5	-
Responsivity	$R(\lambda)\forall\lambda$	0.4	A/W
Receiver bandwidth	B	50	MHz
TIA noise current density	I_{pa}	5	pA/ $\sqrt{\text{Hz}}$

¹ MIMO specific parameter

² SISO specific parameter

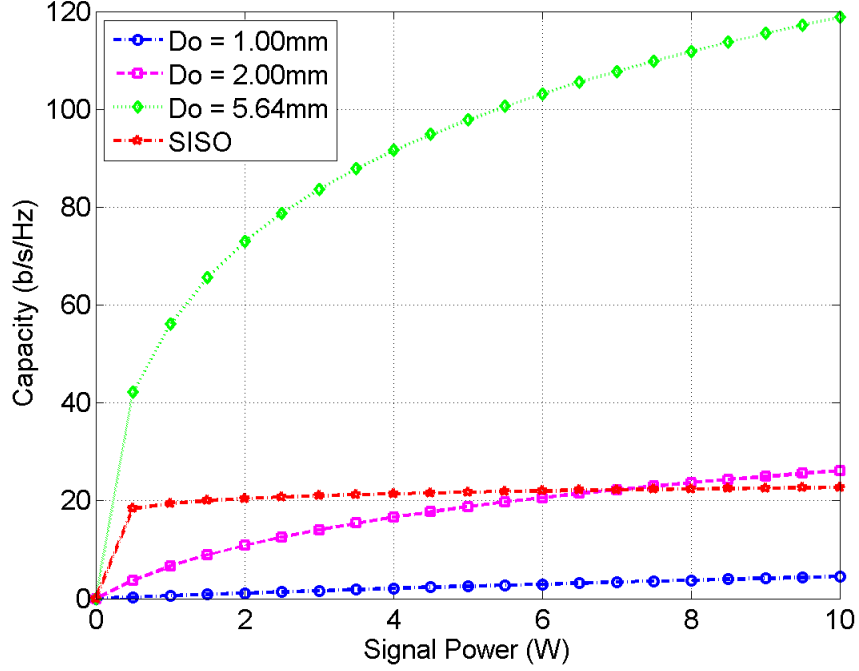


Figure 1-3: Capacity vs Dimming

a range of signal power constraints and different lens aperture diameters when the receiver is at the center of the 1m plane. The capacity of the MIMO VLC channel is then calculated at the same power constraints as a SISO channel. As expected, the capacity of the imaging channel does increase with increasing aperture diameter. At aperture diameter of 5.64mm, the imaging receiver and the SISO receiver collect the same amount of average radiant flux, however the MIMO channel shows high spectral efficiency gains. This gain in capacity can be explained by the introduction of multiple parallel links due to the imaging receiver architecture and the reduction in ambient shot noise per channel as indicated in (Djahani and Kahn, 2000). While the imaging receiver collects the same amount of ambient flux as the SISO receiver, this flux can be assumed to be equally divided among all the pixels on the receiver due to imaging optics. Thus each link has greatly reduced ambient flux, thus reducing the noise and improving the capacity. The limiting factor in this case is the thermal

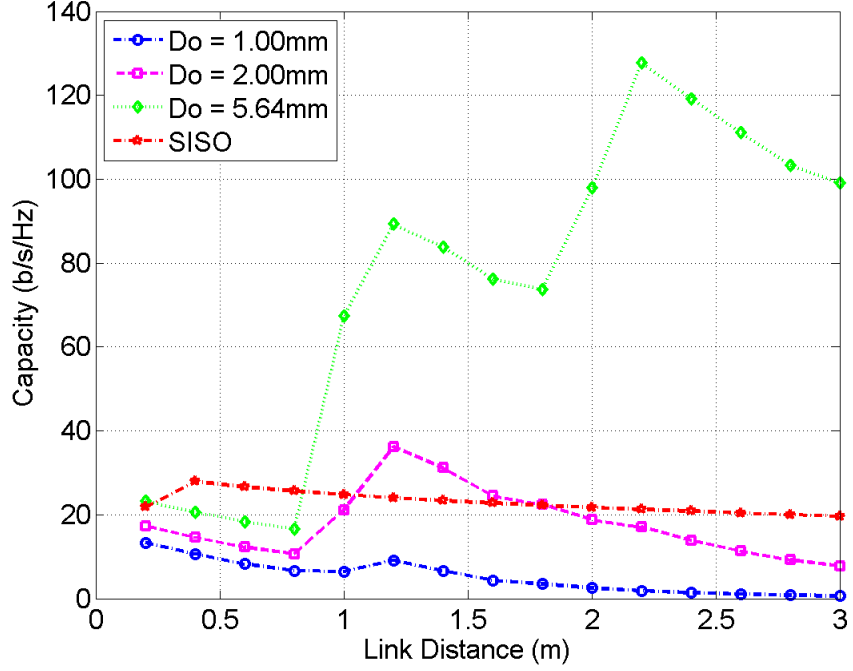


Figure 1-4: Capacity vs Link Distance

noise.

Figure 1-4 shows capacities calculated at different link distances when the total signal power is 5W. The link distance here is defined as the length of a vector from origin of the receiver coordinate system along \hat{z} when it intersects the transmitter plane. The SISO channel capacity monotonically decreases with increasing link distance. The capacity of the MIMO channel goes through regions of positive (increasing) and negative (decreasing) slopes.

As seen in Figure 1-5a, at the 1m link distance, only 1 transmitter is in the receiver's FOV while adjacent transmitters are just outside the FOV. Increasing the link distance to 1.2m causes the adjacent transmitters to enter the receiver FOV, increasing the number of parallel channels as seen in Figure 1-5b. The corresponding increase in capacity is greater than the small decrease caused by the increasing link distance. Thus the MIMO channel capacity curve has a positive slope upto 1.2m.

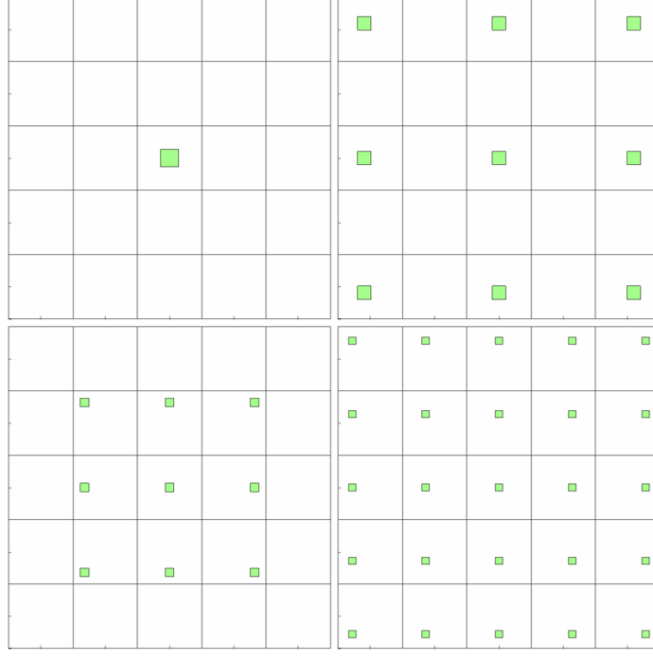


Figure 1-5: Spots (magnified for better illustration) as projected on the imaging receiver sensor plane at different link distances which are (a) top left: 1.0m (b) top right: 1.2m (c) bottom left: 2.0m (d) bottom right: 2.2m

Between 1.2m to 1.8m, number of transmitters seen by receiver remain the same as the link distance is further increased. This causes the capacity of each individual link to decrease thus causing an overall decrease in the channel capacity from 1.2m to 1.8m. Figure 1-5c shows the transmitters projected on the receiver at a link distance of 2.0m where one can see more adjacent transmitters begin to enter the receiver FOV and at 2.2m as in Figure 1-5d, the transmitters are completely in the receiver FOV thus causing an increase in capacity due to more parallel channels. From 2.2m to 2.8m, no more transmitters enter the receiver FOV and thus the overall capacity decreases with increasing link distance.

Having studied the effect of total power constraint and link distance on the capacities of optical channel with imaging receiver, I wish to study the effect of constraints that the receiver orientation poses on the system performance. Also, as the number

Table 1.2: SVD-VLC Simulation Illumination Constraints

Case	Dominant luminaire(s)	400lx Setpoint location
a	1 3 3'	1 3 1'
b	3 1 3'	3 1 1'
c	1 1 3' and 3 3 3'	2 2 1'

of receive pixels increases, so does the need for parallel channels to receive simultaneous streams thus making the receiver more complex. I shall investigate modulation schemes like Spatial Modulation that can benefit from multiple transmitters but reduce the receiver complexity.

To illustrate generation and maintenance of an illumination state using the SVD-VLC architecture, three different scenarios for different illumination states were simulated using SVD-VLC. For these scenarios, the uniform illumination constraint that was relaxed. Table 1.2 now outlines the new illumination constraints. The dominant luminaire(s) column specifies the transmitter(s) whose average output radiant flux was configured to be 20x that as compared to each of the other transmitters. Setpoint location column specifies the location in the room where 400lx illumination is requested. The combination of these two values specifies a unique illumination state for each scenario. The constraints were specified in this manner to prevent an unacceptably high illumination level at any other point on the illumination surface. A more complex illumination state can be imposed as a constraint to generate a particular light field, however this simple case is sufficient to illustrate the SVD-VLC behavior.

Table 1.3: SVD-VLC Simulation Illumination Results

Receiver		Simulated illumination (lx)		
Location	Rank(H)	a	b	c
1.6 0.6 1.0'	16	399.99	400.29	400.22
2.8 0.4 1.4'	12	400.00	401.75	400.00
0.2 0.8 1.0'	12	399.81	399.92	401.26
1.2 1.4 1.6'	9	400.06	400.01	401.97

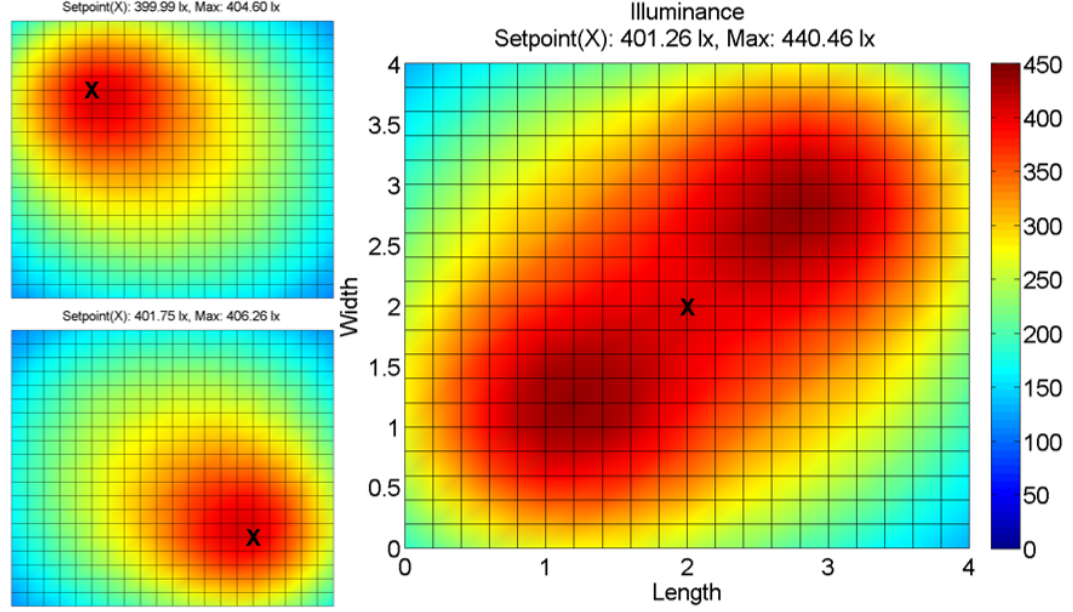


Figure 1.6: Generation and maintenance of illumination state by SVD-VLC. 'X' marks the setpoint location in the illumination plane at 1m height. Scenarios: (a) Top left (b) Bottom left (c) Right

Receiver locations at four different time instants are chosen pseudorandomly to simulate a varying channel matrix due to mobility. For each of the three scenarios, a 1024 length long data sequence was generated from a uniform distributed pseudorandom number sequence in the (0,1) range. The data sequence was scaled to meet the average signal constraint specified by \mathbf{P}' and I1 and I2 streams were generated. After multiplexing these streams over the p-channel, the resulting illumination state was calculated as illustrated in Figure 1.6. Table 1.3 shows values for the illumination achieved at the setpoint location as the channel matrix varies with the receiver's location. It can be seen that despite the variations in the channel matrix, the illumination state remains nearly constant.

1.2 Multi-wavelength system design

1.2.1 Wavelength Division Multiplexing

Different colors including shades of white for illumination on the black body radiation curve can be produced by mixing different amounts of narrow-band SPDs emitted by different sources. The ability to combine multiple narrow-band sources to generate white light also provides the benefit of being able to transmit concurrent information streams over different color groups; thus enabling WDM.

Lasers and LEDs produce a much smaller SPD spread as compared to incandescent and fluorescent sources and are thus preferable for WDM. LED emission can be modeled with a Gaussian distribution as in Eq. (1.11a) while laser emission can be modeled with a Lorentzian distribution as in Eq. (1.11b). Equations in (1.11) model emission spectra for the j^{th} transmitting element.

$$S_j(\lambda) = \frac{1}{\sqrt{2\pi\sigma_j^2}} \exp \left[-\frac{(\lambda - \lambda_j)^2}{2\sigma_j^2} \right] \quad (1.11a)$$

$$S_j(\lambda) = \frac{1}{\pi} \frac{0.5\Gamma_j}{(\lambda - \lambda_j)^2 + (0.5\Gamma_j)^2} \quad (1.11b)$$

where λ_j is the dominant wavelength of emission, σ_j is the measure of spread (deviation) from the dominant wavelength for the Gaussian model, and Γ_j is the FWHM from the dominant wavelength for the Lorentzian model. At small SPD spread, most of the optical power is emitted at the dominant wavelength. At larger SPD spread the optical power is distributed across a larger wavelength range and starts overlapping across different transmitting elements, thus causing interference.

To generate white light $W(\lambda)$, emissions from different transmitting elements are weighted by factor t_j before being mixed together. The resulting spectrum is given

by

$$W(\lambda) = \sum_{j=1}^{N_{tx}} t_j S_j(\lambda) \quad (1.12)$$

The *commission internationale de l'éclairage* (CIE) specified the CIE 1931 XYZ color space. It maps an SPD to a color representation as sensed by the human eye. The standard defines three color matching functions $x_c(\lambda)$, $y_c(\lambda)$, and $z_c(\lambda)$ as shown in Figure 1.7. The tristimulus values for the XYZ primaries are given by

$$X_W = \int_{\lambda_{min}}^{\lambda_{max}} W(\lambda) x_c(\lambda) d\lambda \quad (1.13a)$$

$$Y_W = \int_{\lambda_{min}}^{\lambda_{max}} W(\lambda) y_c(\lambda) d\lambda \quad (1.13b)$$

$$Z_W = \int_{\lambda_{min}}^{\lambda_{max}} W(\lambda) z_c(\lambda) d\lambda \quad (1.13c)$$

A color can be expressed in terms of its chromaticity and luminance. Chromaticity coordinates capture the hue and saturation of the color while luminance captures the

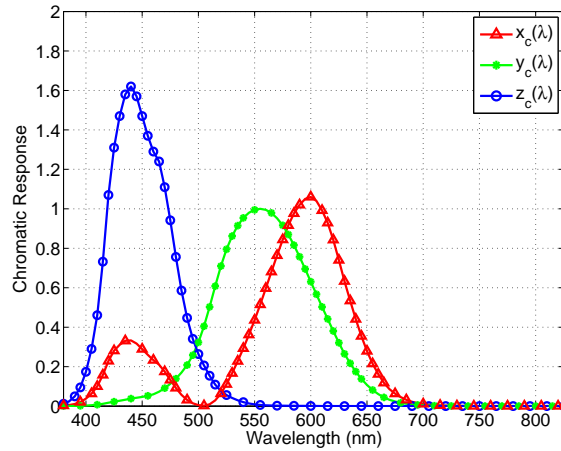


Figure 1.7: CIE XYZ 1931 model color matching functions

amount of light in the color. The chromaticity coordinates for the SPD can be then be computed from the tristimulus values as

$$\begin{bmatrix} x \\ y \end{bmatrix} = \frac{1}{X_W + Y_W + Z_W} \begin{bmatrix} X_W \\ Y_W \end{bmatrix} \quad (1.14)$$

The spectral radiance of a black body heated to temperature T as stated by Planck's law is given by

$$S(\lambda) = \frac{2hc^2}{\lambda^5 \left[\exp\left(\frac{hc}{\lambda kT}\right) - 1 \right]} \quad (1.15)$$

where h is the Planck's constant, c is speed of light, and k is Boltzmann's constant. Replacing $W(\lambda) = S(\lambda)$ in Eq.(1.13) and then from Eq.(1.14) we obtain the CIE 1931 XYZ chromaticity values $[x, y]$ associated with a black body heated to temperature T . In this context T is also known as the CCT for color represented by $[x, y]$. Note that two different SPDs can generate the same chromaticity coordinates. This is due to the principle of metamerism.

Traditionally luminaires have been specified to generate a certain CCT with colors at lower temperature appearing (ironically) warmer than those at higher temperatures. It is practical to generate colors off the black body radiation curve using different colored sources. This analysis considers only the colors generated on the black body radiation curve. As the CCT changes from a lower value to a higher value, the optical power available to transmit information on any color channel varies thus affecting the overall communication performance.

Optical filters can be manufactured to permit narrow-bandpass filtering using plasmonics (Xu et al., 2010; Yokogawa et al., 2012). Broad-bandpass optical filters that make use of interference are widely available. The transmittance of these filters can be modeled as Lorentzian functions of wavelength. The choice of the filter FWHM is a tradeoff to collect the maximum signal while rejecting interference and background

illumination.

Responsivity of the receiving elements also affects the aggregate system performance. It depends on the quantum efficiency of the material of sensor. Reference (Z. Ghassemlooy, 2012) computes responsivity as

$$R(\lambda) = \frac{\xi \lambda}{1240} \quad (1.16)$$

where ξ is the quantum efficiency of the material, and λ is wavelength of interest. For equal signal radiant flux, signals that span wavelength ranges with lower responsivity will perform poorly as compared to the rest.

Optical spectrum outside the visible range like infrared (IR) and ultraviolet (UV) spectrum can also be utilized for WDM. It can be seen from Figure1.7 that IR and UV do not generate chromatic response on human eye and thus do not contribute to visible illumination. Thus, as long as their emissions satisfy eye and skin safety regulations, using this additional optical spectrum can only boost the channel capacity.

1.2.2 Analysis

Simulations are performed to study how the choice of design parameters like illumination CCT, transmitter SPD, and filter FWHM affect the performance of a multi-wavelength VLC system. Three transmitting elements with Gaussian emission spectrum at dominant wavelengths of red (627 nm), green (530 nm) and blue (470 nm) are selected. Using these transmitting elements, CCT range of [2500 7000] K is sought. SPD spread within [5 50] nm is considered. Figure1.8 illustrates normalized SPDs needed to achieve the range of CCTs for transmitting elements with 5 nm spread.

Unique $t_R : t_G : t_B$ ratios are generated after varying the tristimulus values in the range [0 1] in 0.1 unit steps. By substituting these values in Eq.(1.12)-Eq.(1.14), chromaticity coordinates for resulting SPDs are calculated. An initial characteri-

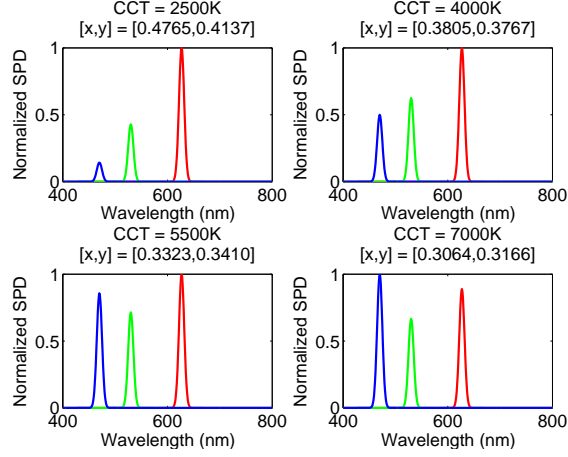


Figure 1-8: Transmitting element normalized spectral power distribution

zation step generates a pre-populated table consisting of the tristimulus values and corresponding chromaticity coordinates. As the CCT is varied, the chromaticity coordinates are pre-computed. From the pre-computed table, the tristimulus values that achieve the closest chromaticity are selected. The SPD is then scaled to achieve target illumination (400 lx) at the receiver that is located at a distance of 2 m from the transmitter. The surface normals of the transmitter and receiver are assumed to be parallel.

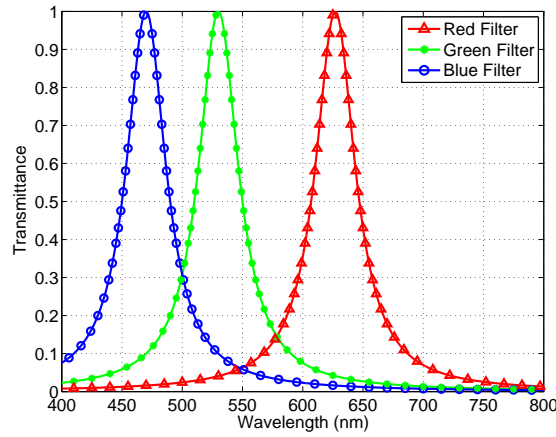


Figure 1-9: Filter transmittance for full width at half maximum = 40nm

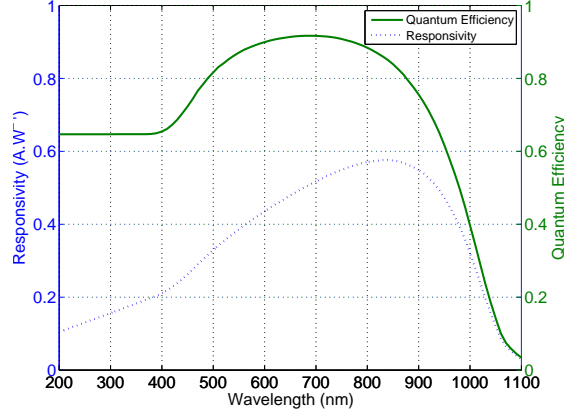


Figure 1-10: Receiver quantum efficiency and responsivity

Optical filter's passband can be designed to center on the transmitting elements' dominant wavelengths. Optical filters for the simulation are modeled to have Lorentzian transmittance with ideal value 1 at the dominant red, green and blue wavelengths mentioned above. Filter transmittance as a function of wavelength is illustrated in Figure1-9. Filter FWHM considered for the analysis lie in [1 250] nm range.

The receiver sensor is assumed to be made of silicon. The assumed quantum efficiencies and responsivity of the sensor taken from online source is illustrated in Figure1-10. The responsivity near the blue wavelength is about 0.29 A.W^{-1} and increases steadily to about 0.46 A.W^{-1} near the red before rapidly reducing as the energy of the incident photon approaches the bandgap energy of silicon.

To analyze the system performance with reasonable number of iterations, transmitting and receiving elements are restricted to the same deviations about their respective means. A random bit stream is then generated. Bits for each link are then communicated using asymmetrically clipped offset and DC-biased optical orthogonal frequency division multiplexing (ACO-OFDM and DCO-OFDM). Details on these optical OFDM techniques can be found in references (Carruthers and Kahn, 1996; Armstrong and Lowery, 2006). For this simulation, ACO-OFDM and DCO-OFDM are implemented with 64 sub-carriers and 64-QAM and 8-QAM modulation, respec-

tively. This ensures that both schemes achieve similar bits/symbol with ACO-OFDM achieving 96 bits/symbol and DCO-OFDM achieving 93 bits/symbol. The DC level on each link is set to ensure the desired CCT is achieved at the 400 lx illumination level. This generates the transmit vector \mathbf{X} .

Having established $N_{tx} = 3$ transmitting and $N_{rx} = 3$ receiving elements, the 3×3 channel matrix \mathbf{H} can be computed. AWGN vector \mathbf{W} is generated and is then added to the transmitted vector. With the knowledge of the transmitted signal power and by varying the receiver noise, simulations over a range of $\text{SNR}_{\text{avg}}^{\text{tx}}$ are carried out. Vector \mathbf{Y} then collects the received signal and the added noise and interference. The least squares estimate of the transmitted signal vector is computed as

$$\hat{\mathbf{X}} = (\mathbf{H}^* \mathbf{H})^{-1} \mathbf{H}^* \mathbf{Y} \quad (1.17)$$

An estimate of the transmitted optical OFDM frame for each color is obtained by aggregating least squares estimates of the received signal vectors. Further signal processing on each optical OFDM frame gets an estimate of the transmitted QAM symbol. Decoding the QAM symbols provides an estimate of the transmitted bits. Bit error rate (BER) is then calculated by comparing the transmit and estimated bit streams.

1.2.3 Results and Discussion

For each unique configuration yielded by varying the parameters, BER versus $\text{SNR}_{\text{avg}}^{\text{tx}}$ is empirically determined using monte-carlo simulations. Based on the simulation setup, the path-loss from the transmitting elements to the receiving elements is about 145 dB. To plot the change in system performance when each parameter is varied, the minimum $\text{SNR}_{\text{avg}}^{\text{tx}}$ needed to achieve target $\text{BER} \leq 10^{-3}$ is selected. Since ACO-OFDM is more power efficient compared to DCO-OFDM, for all the cases discussed

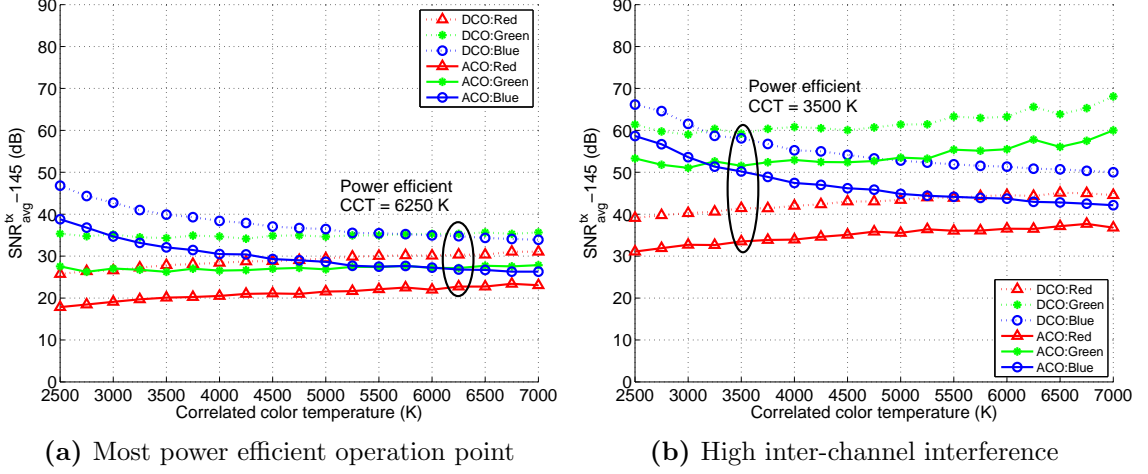


Figure 1.11: $\text{SNR}_{\text{avg}}^{\text{tx}}$ vs correlated color temperature to achieve $\text{BER} \leq 10^{-3}$

- (a) Transmitter: $\sigma_r = \sigma_g = \sigma_b = 5$ nm; Filter: $\Gamma_r = \Gamma_g = \Gamma_b = 40$ nm
- (b) Transmitter: $\sigma_r = \sigma_g = \sigma_b = 50$ nm; Filter: $\Gamma_r = \Gamma_g = \Gamma_b = 250$ nm

below, ACO-OFDM needs lower transmit signal power to achieve the target BER as compared to DCO-OFDM.

The change in performance of the red, green and blue links as the CCT is varied from 2500 K to 7000 K is shown in Figure1-11. At 2500K, the SPD has a greater contribution from red, then green and then blue. Thus the red link achieves target BER at lower transmitted signal power. As the CCT increases, relative signal power from the red link decreases, that of the green remains similar, and that of the blue increases. Thus, with increase in CCT, the amount of aggregate transmit flux needed to achieve target BER from the red link starts increasing, that of the green remains relatively unchanged, while that of the blue decreases. For the specified multi-wavelength system, $\text{CCT} = 6250$ K provides the most power efficient operating point as illustrated in Figure1-11a. Increasing the transmitting elements' SPD or the filter FWHM introduces increasingly more inter-channel interference (ICI). This causes the most power efficient operating point to shift towards $\text{CCT} = 3500$ K but

with greater power requirements as seen in Figure1.11b.

The change in performance of the red, green and blue links as the transmitting element SPD spread is varied from 5 nm to 50 nm is shown in Figure1.12. As the SPD spread is increased, the performance of all three links degrade. This can be attributed to two factors. Initially, as the signal power is distributed across a larger wavelength range, with the filter transmittance function remaining the same, increasingly more signal gets rejected by the filter. Thus the receiver collects a smaller fraction of the signal power, degrading the performance. Secondly, as the individual SPDs spread enough, they start overlapping and causing ICI. The effect of ICI is more pronounced on the green link because it gets interference from both, red and blue. Thus transmitter consisting of transmitting elements with narrower emission spectra are more power efficient than those with wider emission spectra. Experiments in reference (Neumann et al., 2011) qualitatively measure color perception for illumination with narrow-band sources and find lasers could be used for general lighting. However, it is also commonly believed that sources with spiky emission spectra do not produce good quality of illumination because objects with reflectance spectra lying outside

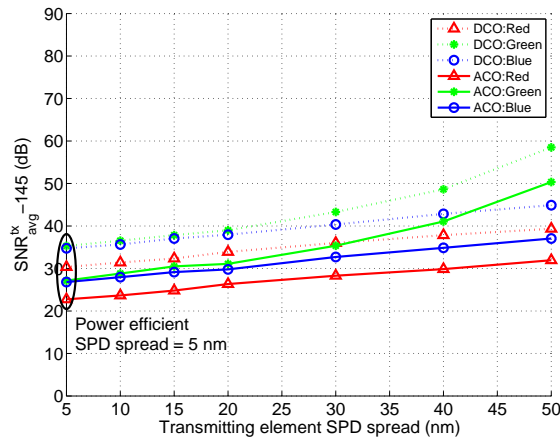


Figure 1.12: $\text{SNR}_{\text{avg}}^{\text{tx}}$ vs transmitting element spectral power distribution spread to achieve $\text{BER} \leq 10^{-3}$

Filter: $\Gamma_r = \Gamma_g = \Gamma_b = 40 \text{ nm}$; CCT = 6250 K

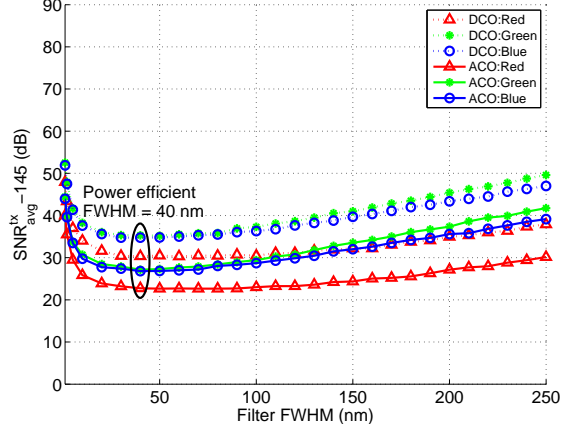


Figure 1.13: $\text{SNR}_{\text{avg}}^{\text{tx}}$ vs filter full width at half maximum to achieve $\text{BER} \leq 10^{-3}$

Transmitter: $\sigma_r = \sigma_g = \sigma_b = 5 \text{ nm}$; CCT = 6250 K

the spikes in the illumination spectra will be perceived to be poorly lit. The choice of the transmitting elements' SPD spread would be a tradeoff between the communication and illumination performance. For the specified multi-wavelength system, SPD spread = 5 nm provides the most power efficient operating point.

The change in performance of the red, green and blue links as the receiving element filter FWHM is varied from 1 nm to 250 nm is shown in Figure1.13. As the filter FWHM increases, initially the system performance improves significantly. At these lower FWHM ranges, the filters transmit a smaller fraction of the signal to the sensors and thus performance is limited by the amount of signal power collected for each link. At higher FWHM ranges, along with additional signal, the filters permit increasingly more ambient light and interference from neighboring links, thus degrading the performance. For the specified multi-wavelength system, filter FWHM = 40 nm provides the most power efficient operating point.

References

- Armstrong, J. and Lowery, A. (2006). Power efficient optical ofdm. *Electronics Letters*, 42(6):370 – 372.
- Carruthers, J. and Kahn, J. (1996). Multiple-subcarrier modulation for nondirected wireless infrared communication. *Selected Areas in Communications, IEEE Journal on*, 14(3):538–546.
- Djahani, P. and Kahn, J. (2000). Analysis of infrared wireless links employing multibeam transmitters and imaging diversity receivers. *Communications, IEEE Transactions on*, 48(12):2077–2088.
- Goldsmith, A. and Varaiya, P. (1997). Capacity of fading channels with channel side information. *Information Theory, IEEE Transactions on*, 43(6):1986–1992.
- Grubor, J., Randel, S., Langer, K.-D., and Walewski, J. (2008). Broadband information broadcasting using led-based interior lighting. *Lightwave Technology, Journal of*, 26(24):3883–3892.
- Neumann, A., Wierer, J. J., Davis, W., Ohno, Y., Brueck, S. R. J., and Tsao, J. (2011). Four-color laser white illuminant demonstrating high color-rendering quality. *Opt. Express*, 19(S4):A982–A990.
- Park, K.-H., chai Ko, Y., and Alouini, M.-S. (2011). A novel power and offset allocation method for spatial multiplexing mimo systems in optical wireless channels. In *GLOBECOM Workshops (GC Wkshps), 2011 IEEE*, pages 823–827.
- Tse, D. and Viswanath, P. (2005). *Fundamentals of wireless communication*. Cambridge University Press, New York, NY, USA.
- Xu, T., Wu, Y.-K., Luo, X., and Guo, L. J. (2010). Plasmonic nanoresonators for high-resolution colour filtering and spectral imaging. *Nature Communications*, 1(59).
- Yokogawa, S., Burgos, S. P., and Atwater, H. A. (2012). Plasmonic color filters for cmos image sensor applications. *Nano Letters*, 12(8):4349–4354.
- Z. Ghassemlooy, W. Popoola, S. R. (2012). *Optical wireless communications: system and channel modelling with MATLAB®*. CRC Press.

Zeng, L., O'brien, D., Le-Minh, H., Lee, K., Jung, D., and Oh, Y. (2008). Improvement of data rate by using equalization in an indoor visible light communication system. In *Circuits and Systems for Communications, 2008. ICCSC 2008. 4th IEEE International Conference on*, pages 678–682.